ACS OMEGA

http://pubs.acs.org/journal/acsodf

Article

Dual-Metal Active Sites Mediated by p-Block Elements: Knowledge-Driven Design of Oxygen Reduction Reaction Catalysts

Pengyue Shan, Xue Bai, Qi Jiang, Yunjian Chen, Yazhou Wang, Tong Liu, Hong Cui,* Rong Feng, Qin Kang, Zhiyong Liang, and Hongkuan Yuan

Cite This: *ACS Omega* 2022, 7, 19676−19686

Read Online

ACCESS | Metrics & More | Article Recommendations | Supporting Information

ABSTRACT: In this study, the oxygen reduction reaction (ORR) process of dual-metal active site catalysts ($FeMN_6$-Gra, M = Mn, Ni, Co, or Cu) mediated by p-block elements was investigated using density functional theory calculations. The obtained results demonstrate that, in most cases, the B-doped $FeMN_6$-Gra (M = Mn, Ni, Co, or Cu) catalysts exhibit higher catalytic performance than their undoped counterparts. Among the investigated catalysts, $FeNiN_6$-Gra doping by B modulates the adsorption strength of the metal center on the oxygen-containing intermediates, showing the largest increase in the onset potential (from 0.66 to 0.94 V). Importantly, we found a new law that B-doping affects the total charge of the metal adsorption site and the four surrounding N atoms and that there is a linear relationship between the total charge and the Gibbs free energy. Transition state analysis shows that the energy barrier of the thermodynamic rate-determining step (*OH hydrogenation to H_2O) in the $FeNiN_6B1$-Gra-catalyzed ORR process is 0.17 eV, which is smaller than that of the $FeNiN_6$-Gra-catalyzed process (0.28 eV). Overall, the results demonstrate that B-doping can improve the activity of $FeMN_6$-Gra catalysts and provide a new method for the future development of efficient electrocatalysts.

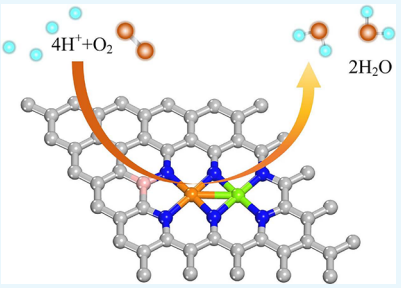

INTRODUCTION

Fuel cells are sustainable energy sources that have received a lot of attention due to their ability to relieve human dependence on non-renewable fossil fuels.[1−3] Unfortunately, the efficiency of these cells is limited by the slow kinetics of the oxygen reduction reaction (ORR) that occurs at the cathode.[4] Therefore, it is necessary to develop more efficient cathode catalysts. In recent decades, noble Pt metals[5] and Pt-based alloys[6,7] have been most widely used as cathode electrocatalysts; however, the high cost of these materials impedes their application in fuel cells on an industrial level. This indicates that low-cost and highly active non-precious metal electrocatalysts are needed.

Recently, atomically dispersed transition metal single-atom catalysts (SACs) have emerged as viable cathode electrocatalysts for use in fuel cells. In particular, the design of highly effective and selective Pt_1/FeO_x single-atom catalysts[8] has inspired new ideas for the improvement of metal utilization. The single metal atom provides a unique modulated active center on the carrier surface, thereby optimizing the activity, selectivity, and stability of multiphase catalysts.[9] TM-N-C materials (TM indicates transition metal) have also been proposed as promising catalysts for ORR. Moreover, studies conducted on TMNx-C show that these materials have good stability and catalytic efficiency for ORR.[10−12] For example, first-principles molecular dynamics (MD) simulations demonstrate that MnN_4-embedded graphene (MnN_4-Gra) is stable at high temperatures and leads to exothermic ORR pathways. Moreover, the catalytic activity of this material is comparable to that of Pt catalysts.[10] Based on experimental studies performed on TM-N co-doped carbon nanotubes (TM-N-CNTs), the Fe-N-CNT half-wave potential is 0.87 V, which has high catalytic activity.[11] Specifically, the experimental activity of FeN_4-doped graphene catalysts is very close to that of commercial 40% Pt/C catalysts.[12] Multistage porous Co−N functionalized graphene aerogels are also effective catalysts for ORR in acidic electrolytes. The high catalytic activity of these materials is attributed to the abundance of active sites available for ORR, which ensures rapid mass transfer during catalysis.[13] CoNx-doped graphene alkenes have particularly high ORR efficiency, and their catalytic mechanisms vary depending on the number of nitrogen atoms.[14]

Compared to monometallic atom catalysts, materials doped with double-transition metal atoms as active sites exhibit improved catalytic activity because of the synergy between the metal atoms. For example, porous carbon co-doped with Fe, Co, and N shows high catalytic activity, and its onset potential and half-wave potential are better than those of the Fe−N−C and Co−N−C monometallic atom catalysts.[15] The working

Received: March 9, 2022
Accepted: May 20, 2022
Published: June 3, 2022

https://doi.org/10.1021/acsomega.2c01415
ACS Omega 2022, 7, 19676−19686

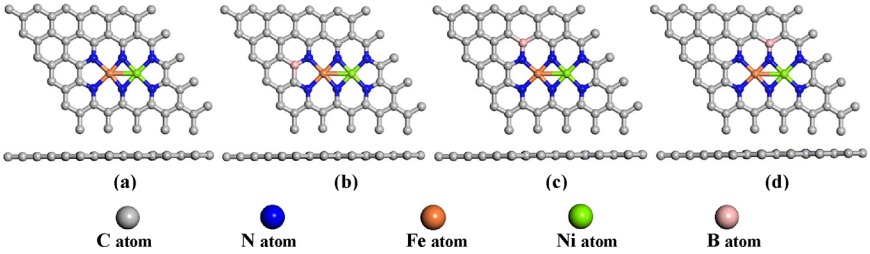

Figure 1. Geometry optimization of B-doped $FeMN_6$-Gra catalysts. (a) $FeNiN_6$-Gra, (b) $FeNiN_6B1$-Gra, (c) $FeNiN_6B2$-Gra, and (d) $FeNiN_6B3$-Gra.

potential and energy barrier of $FeCoN_6$-Gra are 0.97 and 0.34 eV, even better than Pt (0.78 and 0.80 eV, respectively).[16] Moreover, theoretical studies reveal that $FeCoN_7$ and $FeCoN_8$ sites have a minimum overpotential of 0.22 V.[17] Similarly, Fe, Mn, and N co-doped graphene exhibit superior catalytic activity compared to Pt/C and catalysts composed of Fe−Nx active sites.[18] Based on density functional theory calculations, bimetallic active centers, including PGM (Pt and Pd) and non-PGM (Fe, Co, Ni, and Cu) metals embedded in graphene monolayers and coordinated by six pyridine nitrogen atoms, exhibit high catalytic activity for ORR due to the effect of the second metal site in promoting the O−O bond cleavage in the OOH* intermediate, which alleviates the *OH removal problem.[19,20]

To improve the activity of ORR catalysts, researchers have also developed materials wherein more than one nonmetallic atoms is added to the metal-atom catalyst.[21−25] Using the nacl-template pyrolysis method, single Fe atom catalysts with atomically dispersed Fe-heteroatom (N and S) bridge sites anchored on carbon nanosheets were experimentally designed. The N- and S-coordinated Fe atom sites (FeN_3S) induce charge redistribution and reduce the oxygen-containing reaction binding strength of intermediates.[21] Density functional theory (DFT) calculations of the oxygen reduction reaction on both sides of the active center in S-doped CoN_4-G catalysts show that these catalysts reduce the overpotential of the ORR.[22] Based on structure−property relationship analyses, the local structures of these catalysts at the molecular level, including the first and second coordination spheres (CSs), synergistically determine the electrocatalytic reaction. The catalytic performance may be adjusted by modifying the first (N or/and O coordination) and second (C−O−C groups) CSs.[23] Shang et al.[24] proposed a practical strategy for the rational design of catalysts composed of individual copper atoms coordinated with sulfur and nitrogen in multilayer porous carbon (S-Cu-ISA/SNC). An atomic interface strategy for the construction of single-atom copper catalysts (Cu-SA/SNC) with high ORR activity in alkaline media and 0.893 V half-wave potential is also reported by Jiang et al.[25] By modulating the d-band center of single-atom catalysts, boron dopants can enhance the efficiency of these catalysts, so much so that it exceeds the efficiencies of pure Fe−N−C and industrial Pt/C in 0.1 M KOH media with a reversible hydrogen electrode (with respect to RHE). First-principles calculations indicate that the d-band center modulated by B-doping provides the system with good oxygen adsorption energy and low overpotential.[26]

In this study, we use DFT calculations to investigate the ORR catalyst design of dual-metal active sites mediated by p-block elements (boron atoms). The effect of B-doping on $FeMN_6$-Gra (M = Mn, Ni, Co, or Cu) catalysts under acidic conditions is analyzed thermodynamically and kinetically, and the mechanism underlying the enhanced catalytic activity for ORR is revealed.

COMPUTATIONAL METHODS

All DFT calculations were conducted using the Vienna ab initio simulation package.[27−29] The monolayer of graphene 5 × 5 sheet doped with $FeMN_6$/$FeMN_6B$-Gra as the model of graphene-based catalysts (Figure 1). The projector-augmented wave method[30] was used to describe the core electrons, and the generalized gradient approximation function implemented in the Perdew−Burke−Ernzerhof generalization was used to exchange the correlated energy generalization.[31] The cutoff energy was set to 500 eV. The Brillouin zones were sampled during structure calculation using 3 × 3 × 1 Monkhorst−Pack meshes.[32] To avoid periodic interactions, a sufficient vacuum of 20 Å was implemented. The convergence criterion for the self-consistent iteration was set at 1×10^{-6} eV, which means that ion relaxation stops when the force on each atom is less than 0.02 eV/Å. Grimme's DFT-D3 theory was employed to account for the van der Waals interactions between adsorbates and substrates.[33] The minimum energy pathway was obtained using the climbing image nudged elastic band method[34] and MD simulations with a time step of 2 fs using DFTB.[35]

The Gibbs free energy change (ΔG) was calculated based on the standard hydrogen electrode model,[36] as shown in eq 1

$$\Delta G = \Delta E + \Delta EZPE - T\Delta S + \Delta GU + \Delta GpH \quad (1)$$

where ΔE, $\Delta EZPE$, and ΔS represent the changes in adsorption energy, zero-point energy correction, and entropy, respectively (calculated based on density functional theory), and T represents the temperature (298.15 K). $\Delta GU = -neU$, where U is the applied electrode potential, e is the transferred charge, and n is the number of proton−electron pairs.

The ORR process occurring in acidic media is given below

$$O_2 + 4(H^+ + e^-) \rightarrow 2H_2O \quad (2)$$

and it involves four steps

$$\Delta G_1: {}^*+O_2 + 4(H^+ + e^-) \rightarrow {}^*OOH + 3(H^+ + e^-) \quad (2a)$$

$$\Delta G_2: {}^*OOH + 3(H^+ + e^-) \rightarrow {}^*O + H_2O + 2(H^+ + e^-) \quad (2b)$$

$$\Delta G_3: {}^*O + H_2O + 2(H^+ + e^-) \rightarrow {}^*OH + H_2O + (H^+ + e^-) \quad (2c)$$

$$\Delta G_4: {}^*OH + H_2O + (H^+ + e^-) \rightarrow 2H_2O + {}^* \quad (2d)$$

https://doi.org/10.1021/acsomega.2c01415
ACS Omega 2022, 7, 19676−19686

The overpotential is given by

$$\eta_{ORR} = 1.23 + \min(\Delta G_1, \Delta G_2, \Delta G_3, \Delta G_4)/e \quad (3)$$

The Gibbs adsorption free energies of H_2O and H_2 were determined based on the ΔG values of the *OOH, *O, and *OH intermediates in ORR, as shown in eqs 4−6, respectively

$$\Delta G_{*OOH} = G_{*OOH} + 3/2G_{H_2} - 2G_{H_2O} \quad (4)$$

$$\Delta G_{*O} = G_{*O} + G_{H_2} - G_{H_2O} \quad (5)$$

$$\Delta G_{*OH} = G_{*OH} + 1/2G_{H_2} - G_{H_2O} \quad (6)$$

where * is the adsorption state of oxygen-containing intermediates, ΔG_{*OOH}, ΔG_{*O}, and ΔG_{*OH} are the free energies of adsorption of *OOH, *O, and *OH, respectively, and G_{H2O} and G_{H2} are the free energies of H_2O and H_2 molecules in the gas phase, respectively.

RESULTS AND DISCUSSION

Stability and Electronic Properties of $FeMN_6$/$FeMN_6$B-Gra Structures. Figure 1 shows the optimized structures of the $FeNiN_6$/$FeNiN_6$B-Gra catalysts, where all atoms are kept in the same plane, and no significant bulges appear. This indicates that these structures have high stability.

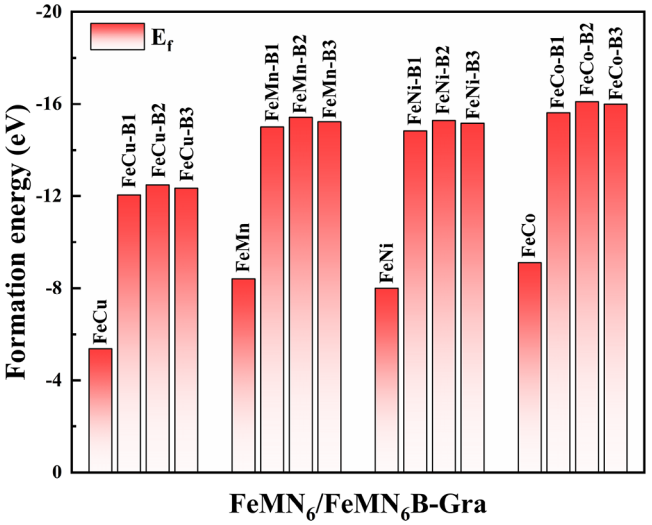

Figure 2. Formation energies of $FeMN_6$ and $FeMN_6$B-Gra catalysts.

The formation energies of $FeMN_6$-Gra (ΔE_{f1}) and $FeMN_6$B-Gra (ΔE_{f2}) are given by the following equations:

$$\Delta E_{f1} = E_{FeMN_6\text{-Gra}} + 10\mu_c[E_{Gra} + 6\mu_N + \mu_{Fe} + \mu_M] \quad (7)$$

$$\Delta E_{f2} = E_{FeMN_6B\text{-Gra}} + 11\mu_c[E_{Gra} + 6\mu_N + \mu_{Fe} + \mu_M + \mu_B] \quad (8)$$

where $E_{FeMN6\text{-Gra}}$ and $E_{FeMN6B\text{-Gra}}$ are the total energies of $FeMN_6$-Gra and $FeMN_6$B-Gra, respectively, and E_{Gra} is the total energy of pure graphene. μ_c is the chemical potential of carbon atoms in monolayer graphene, and μ_N, μ_B, μ_{Fe}, and μ_M represent the chemical potential of the corresponding atom.

The stability of $FeMN_6$/$FeMN_6$B-Gra catalysts was evaluated by calculating their formation energies. The results illustrated in Figure 2 demonstrate that both $FeMN_6$ and $FeMN_6$B-Gra are thermodynamically stable. Moreover, $FeMN_6$B-Gra has a lower formation energy than $FeMN_6$-Gra, which indicates that boron exhibits a strong covalent interaction that enhances the thermodynamic stability of the system.

Table 1. Charge Transfer of Fe, M, and B in $FeMN_6$/$FeMN_6$B-Gra (e) and d/p-Band Center (eV)

model	charge of M	charge of B	d-band center (M)	p-band center (B)
FeCu	+1.14		−2.64	
FeCu-B1	+1.19	+1.93	−2.55	−4.92
FeCu-B2	+1.21	+1.89	−2.83	−5.08
FeCu-B3	+1.18	+1.93	−2.59	−4.26
FeMn	+0.93		−1.92	
FeMn-B1	+0.94	+1.93	−2.07	−4.75
FeMn-B2	+0.97	+1.90	−2.05	−4.37
FeMn-B3	+1.09	+1.90	−2.03	−4.74
FeNi	+1.00		−1.35	
FeNi-B1	+1.20	+1.94	−2.48	−4.70
FeNi-B2	+1.21	+1.89	−2.57	−4.32
FeNi-B3	+1.21	+1.92	−2.58	−4.07
FeCo	+0.98		−1.79	
FeCo-B1	+1.12	+1.93	−2.33	−4.84
FeCo-B2	+1.11	+1.90	−2.36	−4.45
FeCo-B3	+1.03	+1.89	−1.69	−4.78

Based on Bader charge analysis, both the metal and boron atoms are positively charged due to the loss of electrons. The charge transfer from metal atoms at the adsorption sites of oxygen-containing intermediates increases after doping with boron (Table 1), which indicates that B atoms promote the transfer of electrons from metal atoms through the synergistic effect. The M denotes the metal atom of the adsorption site, where the adsorption sites of FeNi, FeCo, and FeCu catalysts are Fe atoms and the adsorption sites of FeMn catalysts are Mn atoms.

Electrocatalytic Performance of ORR. Based on the DFT calculations, the oxygen-containing intermediates *OOH, *O, and *OH in $FeMN_6$/$FeMN_6$B-Gra catalysts tend to adsorb at the top positions of low electronegativity metal atoms. Figure S1 shows the most stable adsorption conformations of these catalysts. To investigate the catalytic performance of the $FeMN_6$/$FeMN_6$B-Gra catalysts, we analyzed the four electron transfer steps implicated in the ORR process, plotted the adsorption energy of these steps, and labeled the onset potentials ($U_{onset\ potential}$) (Figure 3). Table 2 summarizes the adsorption energy and overpotential values corresponding to the oxygen-containing intermediates produced during the ORR processes catalyzed by $FeMN_6$/$FeMN_6$B-Gra.

Figure 3 reveals that the formation of the second water molecule in the ORR process is the rate-determining step for (a) $FeNiN_6$-Gra, (b) $FeCuN_6$-Gra, and (d) $FeMnN_6$-Gra catalysts. Meanwhile, for (c) $FeCoN_6$-Gra catalysts, the rate-determining step is the formation of *OOH. The effect of B-doping on catalytic activity and adsorption properties varies depending on the nature of M. In the case of $FeNiN_6$-Gra (M = Ni), B-doping makes the *OH more easily hydrogenated. The doping also increases the onset potential of the B1 site to 0.94 V. For $FeCuN_6$-Gra catalysts, B1 and B2 site doping reduce the intensity of active center adsorption to *OH and enhance ORR performance compared to the initial structure. B-doping in $FeCoN_6$-Gra catalysts promotes the hydro-

https://doi.org/10.1021/acsomega.2c01415
ACS Omega 2022, 7, 19676−19686

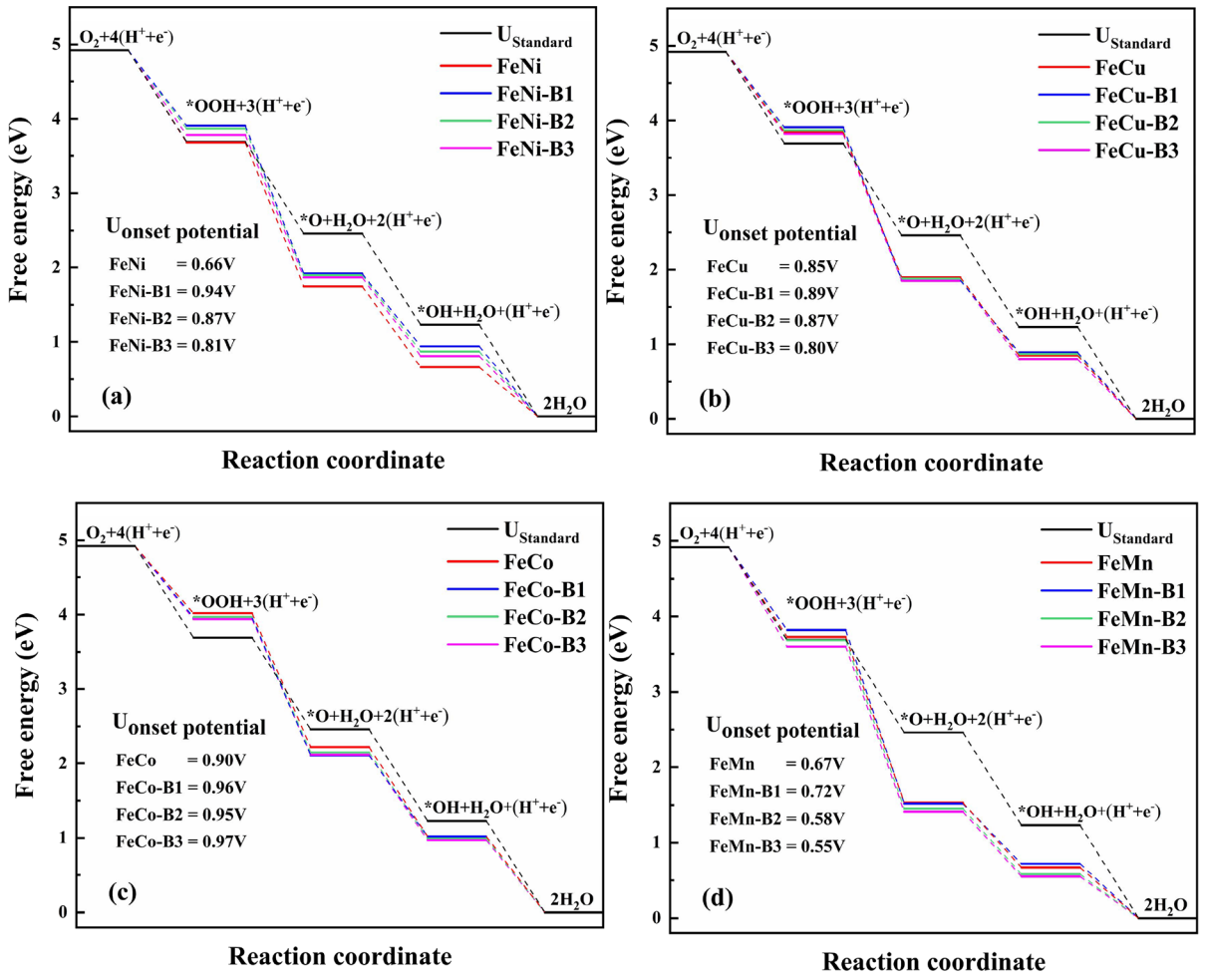

Figure 3. Free energy diagram of the $FeMN_6$/$FeMN_6$B-Gra-catalyzed ORR processes at the onset potential. (a) $FeNiN_6$/$FeNiN_6$B-Gra, (b) $FeCuN_6$/$FeCuN_6$B-Gra, (c) $FeCoN_6$/$FeCoN_6$B-Gra, and (d) $FeMnN_6$/$FeMnN_6$B-Gra.

Table 2. Adsorption Energy and Overpotential (η) of $FeMN_6$/$FeMN_6$B-Gra Oxygen-Containing Intermediates

model	ΔG_{*OOH} (eV)	ΔG_{*O} (eV)	ΔG_{*OH} (eV)	η
FeCu	3.84	1.90	0.85	0.38
FeCu-B1	3.91	1.86	0.89	0.34
FeCu-B2	3.87	1.88	0.87	0.36
FeCu-B3	3.82	1.85	0.80	0.43
FeMn	3.73	1.53	0.67	0.56
FeMn-B1	3.82	1.52	0.72	0.51
FeMn-B2	3.68	1.45	0.58	0.65
FeMn-B3	3.60	1.41	0.55	0.68
FeNi	3.68	1.75	0.66	0.57
FeNi-B1	3.91	1.92	0.94	0.29
FeNi-B2	3.87	1.90	0.87	0.36
FeNi-B3	3.78	1.87	0.81	0.42
FeCo	4.02	2.22	1.02	0.33
FeCo-B1	3.96	2.11	1.02	0.27
FeCo-B2	3.97	2.15	0.99	0.28
FeCo-B3	3.94	2.12	0.97	0.26

genation of O_2 to *OOH. The best catalytic activity is observed at the B3 site whose onset potential is 0.97 V. As for the active center in $FeMnN_6$-Gra catalysts, its adsorption to *OH is undermined by B1 site doping, and its onset potential is increased to 0.72 V.

The above analysis shows that, compared to the other catalysts, $FeNiN_6$-Gra exhibits the largest increase in catalytic activity after B-doping, with an onset potential increase of 0.28 V. Moreover, the overpotential of $FeNiN_6$B1-Gra is only 0.29 V, which is much lower than that of the platinum catalyst (0.45 V). Among the investigated materials, $FeCoN_6$B3-Gra shows the best catalytic activity, with an overpotential of only 0.26 V. These results suggest that B-doping of $FeMN_6$-Gra catalysts is an effective means of improving the efficiency of ORR catalysis.

The effects of other B-doping sites on the catalytic activity were also considered, and the B4 and B5 site doped $FeNiN_6$-Gra and $FeCoN_6$-Gra structures were calculated (Figure S2) with the Gibbs free energy and overpotential shown in Table S1. The results show that the overpotentials of $FeNiN_6$B4-Gra and $FeNiN_6$B5-Gra structures are 0.48 and 0.40 V, respectively, which increase the onset potential compared to the $FeNiN_6$-Gra structure but are lower than the B1 and B2 sites, indicating that B-doping away from the metal adsorption site reduces the modulation effect. The overpotentials of $FeCoN_6$B4-Gra and $FeoN_6$B5-Gra structures are 0.61 and 0.56 V, respectively, and B4 and B5 site doping reduce the starting potential of the catalysts. Therefore, B-doping at the closest position to the metal adsorption site would better improve the catalytic activity of the catalysts.

https://doi.org/10.1021/acsomega.2c01415
ACS Omega 2022, 7, 19676−19686

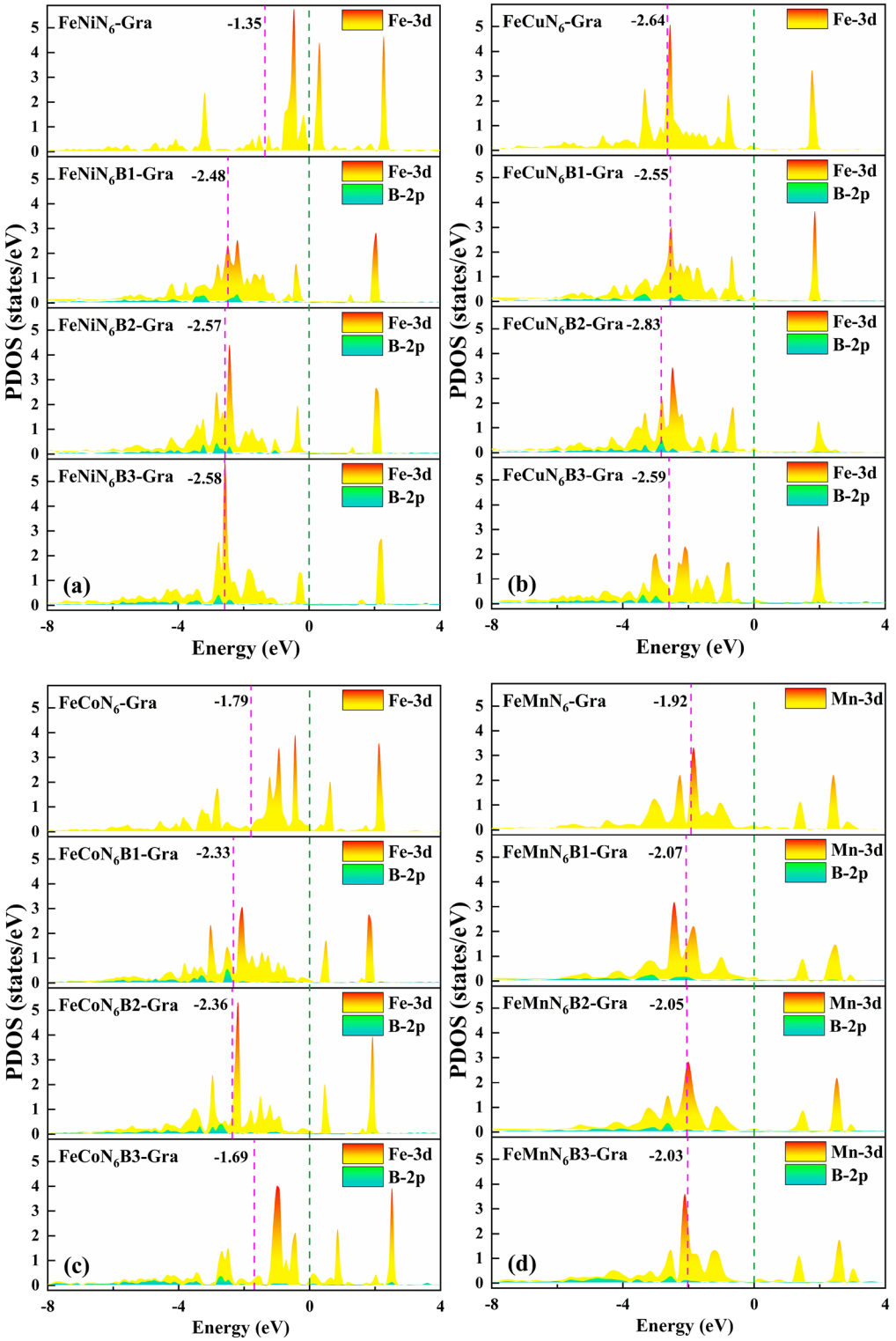

Figure 4. Partial density of states on $FeMN_6$/$FeMN_6$B-Gra. (a) $FeNiN_6$/$FeNiN_6$B-Gra, (b) $FeCuN_6$/$FeCuN_6$B-Gra, (c) $FeCoN_6$/$FeCoN_6$B-Gra, and (d) $FeMnN_6$/$FeMnN_6$B-Gra. The number in the figure is the value of the d-band center. The d-band center of Fe is marked by magenta dotted lines.

To analyze the reason for the p-block element doping, to improve the catalytic performance, the PDOS of the catalysts is shown in Figure 4. The interactions between the metal atoms and B atoms at the adsorption sites are considered, where the adsorption sites of FeNi, FeCo, and FeCu catalysts are all Fe atoms, while the adsorption sites of FeMn catalysts are Mn atoms. As shown in Figure 4a, the d-band center of Fe shifts in the negative direction after $FeNiN_6$-Gra is doped by B atoms, and the Fe-3d peak near the Fermi level decreases, but there is no obvious gap between different B-doping sites. There is no obvious shift of the d-band center in Figure 4b, and the enhancement of catalytic activity is small. In Figure 4c, the d-

https://doi.org/10.1021/acsomega.2c01415
ACS Omega 2022, 7, 19676−19686

Table 3. Total Charge and Free Energy of Adsorption of Oxygen-Containing Intermediates for $FeMN_6$/$FeMN_6$B-Gra

model	total charge	ΔG_{*OH}(eV)	ΔG_{*OOH} (eV)
FeCu	31.35	0.85	
FeCu-B1	31.52	0.89	
FeCu-B2	31.37	0.87	
FeCu-B3	31.28	0.80	
FeMn	36.33	0.67	
FeMn-B1	36.41	0.72	
FeMn-B2	36.30	0.58	
FeMn-B3	36.26	0.55	
FeNi	31.12	0.66	
FeNi-B1	31.42	0.94	
FeNi-B2	31.31	0.87	
FeNi-B3	31.23	0.81	
FeCo	31.07		4.02
FeCo-B1	31.46		3.96
FeCo-B2	31.34		3.97
FeCo-B3	31.55		3.94

band centers of $FeCoN_6$B1-Gra and $FeCoN_6$B2-Gra catalysts are shifted to the left and the peaks at the Fermi level are reduced, while the d-band centers of $FeCoN_6$B3-Gra catalysts are slightly shifted to the right. The PDOS of the B-doped $FeMnN_6$-Gra catalyst in Figure 4d is almost identical, leading to similar activity. In the above analysis, it can be found that the root cause of the increased catalytic activity could not be analyzed by PDOS and the d-band center.

In this paper, B replaces the C atom far from the metal center instead of changing the N atom near the metal, so the different B sites have little effect on the d-band center of the metal to draw accurate analytical conclusions. To find the root cause of B-doping, to improve the catalytic activity, further studies revealed that B-doping affects the total charge of the four N atoms at and near the metal adsorption site, thus affecting the adsorption strength of the oxygen-containing intermediates, as shown in Table 3. In $FeMN_6$/$FeMN_6$B-Gra (M = Ni, Cu, and Mn), the factor that determines the starting potential is the adsorption strength of OH, and it was found that the total charge of the metal atom at the adsorption site and the four surrounding N atoms during OH adsorption has a good linear fit with ΔG_{*OH} of the catalyst (Figure 5). Meanwhile, in $FeCoN_6$/$FeCoN_6$B-Gra, the determining factor is the formation of OOH, and it was found that the total charge of the metal atom at the adsorption site and the four

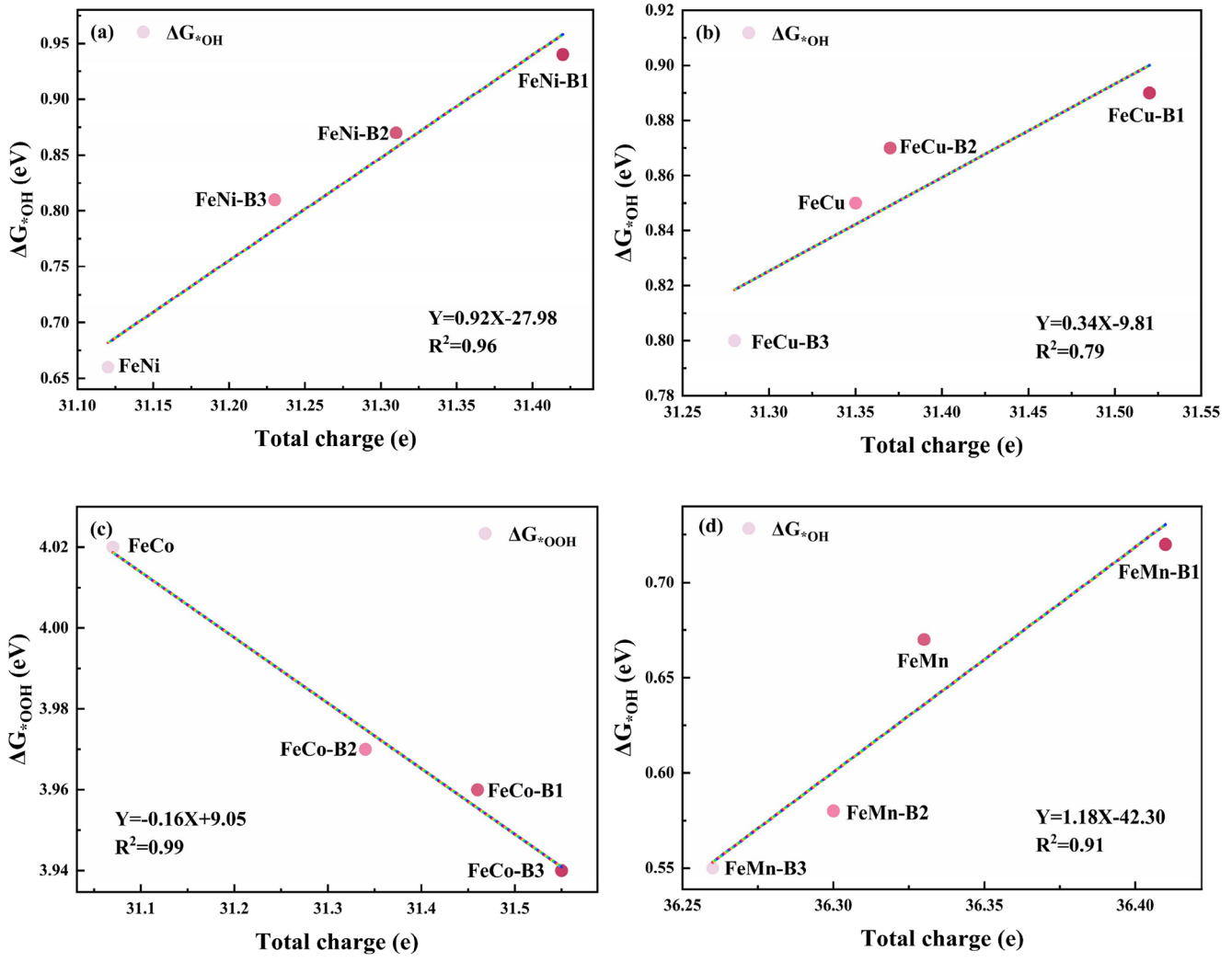

Figure 5. Linear relationship between the total charge of $FeMN_6$/$FeMN_6$B-Gra and the free energy of adsorption of oxygen-containing intermediates. (a) $FeNiN_6$/$FeNiN_6$B-Gra, (b) $FeCuN_6$/$FeCuN_6$B-Gra, (c) $FeCoN_6$/$FeCoN_6$B-Gra, and (d) $FeMnN_6$/$FeMnN_6$B-Gra.

https://doi.org/10.1021/acsomega.2c01415
ACS Omega 2022, 7, 19676−19686

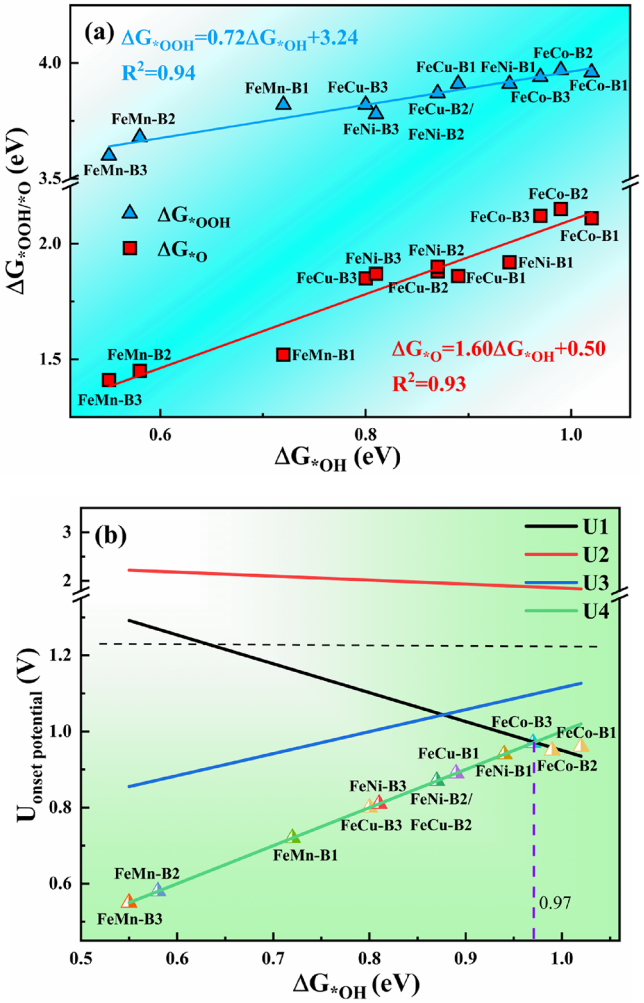

Figure 6. (a) Scaling relationships between the adsorption energy ΔG_{*OH} and $\Delta G_{*OOH}/\Delta G_{*O}$ for $FeMN_6B$-Gra oxygen-containing intermediates. Thermodynamic volcano curves showing the relationships between (b) ORR activity and ΔG_{*OH}.

surrounding N atoms during the adsorption of OOH by $FeCoN_6/FeCoN_6B$-Gra has a better linear fit to the ΔG_{*OOH} of the catalyst (Figure 5).

In the $FeNiN_6/FeNiN_6B$-Gra structure in Figure 5a, the total charge has a very good linear relationship with ΔG_{*OH} (R^2 = 0.96), and as the total charge increases, ΔG_{*OH} increases, weakening the adsorption strength of OH and reducing the overpotential of the catalyst. In Figure 5b, the $FeCuN_6/FeCuN_6B$-Gra adsorption site is a Fe atom and the factor affecting the onset potential is the OH adsorption overpotential, so the total charge of the Fe atom and the four surrounding N atoms during OH adsorption was calculated and it was found that the total charge has a good linear relationship with ΔG_{*OH} (R^2 = 0.79), and the conclusion is consistent with the $FeNiN_6/FeNiN_6B$-Gra; as the total charge increased, ΔG_{*OH} increased, weakening the adsorption strength of OH and reducing the overpotential of the catalyst. In Figure 5c, the $FeCoN_6/FeCoN_6B$-Gra adsorption site is the Fe atom and the factor affecting the onset potential is the formation of OOH, so the total charge of the Fe atom and the four surrounding N atoms during the adsorption of OOH is calculated and it is found that the total charge has a very good linear relationship with ΔG_{*OOH} (R^2 = 0.99), and as the total charge increases, ΔG_{*OOH} decreases, increasing the onset potential of the oxygen reduction reaction. In Figure 5d, the $FeMnN_6/FeMnN_6B$-Gra adsorption site is the Mn atom and the factor affecting the onset potential is too strong OH adsorption, so the total charge of the Mn atom and the four surrounding N atoms during OH adsorption is calculated and it is found that the total charge has a good linear relationship with ΔG_{*OH} (R^2 = 0.91), and as the total charge increases, ΔG_{*OH} increases. The adsorption strength of OH is weakened, and the overpotential of the catalyst is reduced.

The above analysis indicates that B-doping modulates the total charge of the metal at the adsorption site and the four surrounding N atoms during the adsorption of oxygen-containing intermediates, thus changing the adsorption strength of oxygen-containing intermediates and increasing the starting potential, and there is a good linear relationship between the total charge and the Gibbs free energy.

Thermodynamic ORR Activity Relationship. Based on the DFT calculations discussed above, the relationships between the adsorption Gibbs free energies of oxygen-containing intermediates *OOH, *O, and *OH were analyzed. The relationship curves shown in Figure 6a demonstrate that ΔG_{*OH} and ΔG_{*OOH} and ΔG_{*OH} and ΔG_{*O} exhibit linear proportionality. ΔG_{*OOH} and ΔG_{*O} can both be described by functions about ΔG_{*OH}, with $\Delta G_{*O} = 1.60\Delta G_{*OH} + 0.50$ (coefficient of determination R^2 = 0.93) and $\Delta G_{*OOH} = 0.72\Delta G_{*OH} + 3.24$ (R^2 = 0.94). This confirms that the relationship between ΔG_{*OH} and $\Delta G_{*O}/\Delta G_{*OOH}$ is strongly linear and that ORR activity can be described by the ΔG_{*OH} descriptor.

To obtain the relationship between ΔG_{*OH} and the equilibrium potential (U_x) in the ORR process, ΔG_x is taken to be 0 in (eqs 2a–2d). This results in the following equations:

$$eU_1 = \Delta G_{O_2} - \Delta G_{*OOH} \quad (9)$$

$$eU_2 = \Delta G_{*OOH} - \Delta G_{*O} \quad (10)$$

$$eU_3 = \Delta G_{*O} - \Delta G_{*OH} \quad (11)$$

$$eU_4 = \Delta G_{*OH} - \Delta G_{*H_2O} \quad (12)$$

According to the linear relationships described previously, ΔG_{*OH} can be used instead of ΔG_{*OOH} and ΔG_{*O} to obtain the thermodynamic volcanic curve between ΔG_{*OH} and ORR activity (Figure 6b).

As shown in Figure 6b, the rate-determining step in the ORR process is determined based on ΔG_{*OH}. The best ORR activity, i.e., maximum in the volcano plot, is achieved at ΔG_{*OH} = 0.97 eV. $FeCoN_6B3$-Gra, $FeCoN_6B1$-Gra, $FeCoN_6B2$-Gra, and $FeNiN_6B1$-Gra are candidate catalysts with moderate *OH adsorption strength. U1 and U4 also affect the catalytic activity and rate-determining step of ORR. The catalysts showing strong *OH adsorption (*OH < 0.97 eV) ($FeMN_6/FeMN_6B$-Gra, M = Ni, Mn, or Cu, and $FeCoN_6B3$-Gra) are close to U4, which indicates that the formation of the second H_2O in the ORR process is the rate-determining step. Meanwhile, the catalysts showing weak *OH adsorption (*OH > 0.97 eV) ($FeCoN_6B$-Gra, $FeCoN_6B1$-Gra, and $FeCoN_6B2$-Gra) are close to U1, which suggests that the formation of *OOH by hydrogenation of O_2 is the rate-determining step. These results are consistent with the free energy changes seen in Figure 3. Overall, the results illustrated in Figure 6b

https://doi.org/10.1021/acsomega.2c01415
ACS Omega 2022, 7, 19676−19686

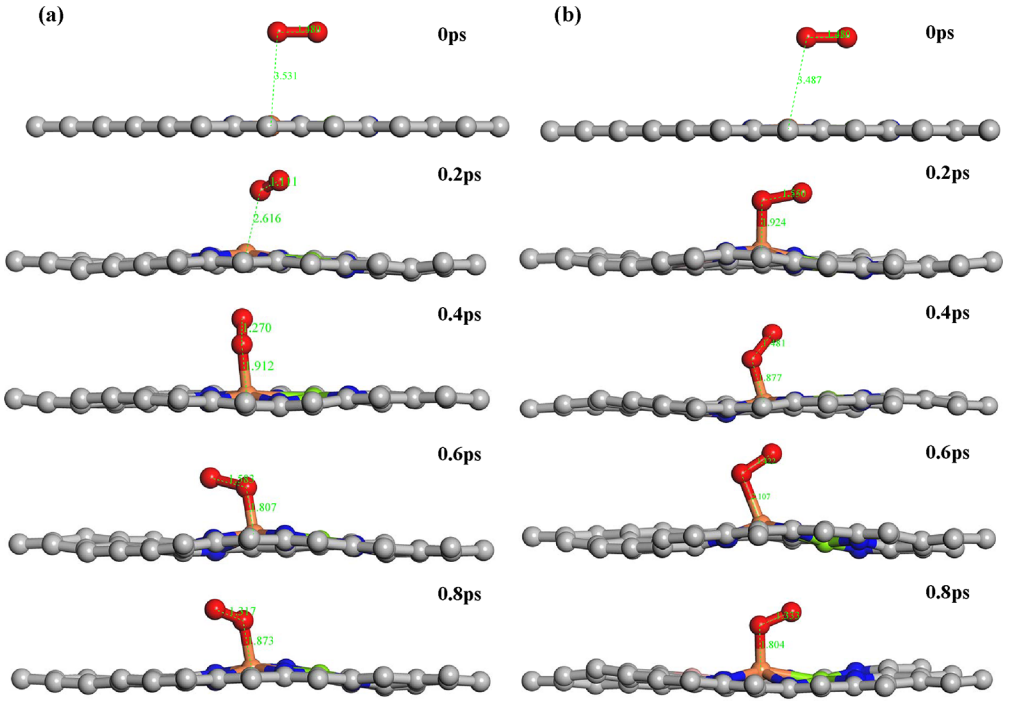

Figure 7. Molecular dynamics simulation of O_2 adsorption on the surface of (a) $FeNiN_6$-Gra and (b) $FeNiN_6B1$-Gra catalysts at 350 K.

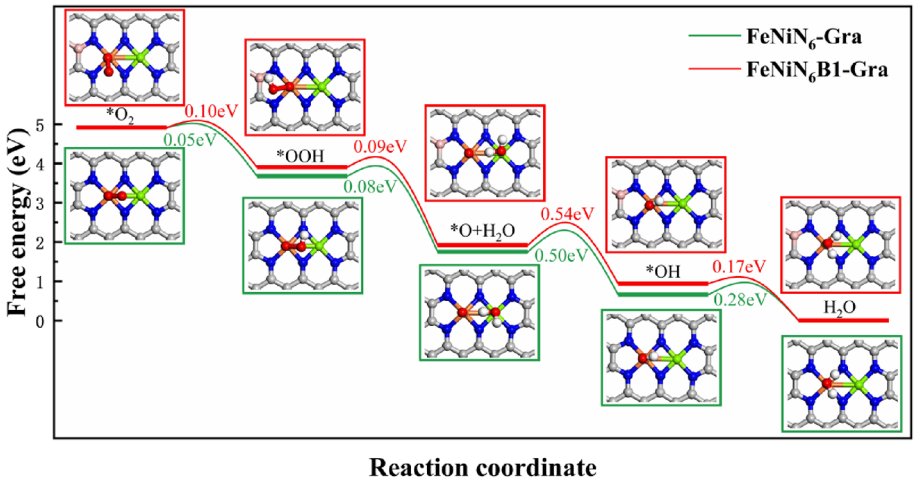

Figure 8. ORR reaction pathways of $FeNiN_6$-Gra and $FeNiN_6B1$-Gra (the numbers are the reaction energy barrier in unit of eV).

demonstrate that the overpotential is related to the adsorption strength of *OH in most cases.

Kinetic Properties of $FeNiN_6$-Gra and $FeNiN_6B1$-Gra. Since the four-electron process did not analyze the adsorption of O_2 on the catalyst surface, to demonstrate that O_2 can spontaneously adsorb on the catalyst surface to participate in the ORR, this section uses molecular dynamics simulations of the reaction of O_2 on $FeNiN_6$-Gra and $FeNiN_6B1$-Gra catalysts indicated at a temperature of T = 350 K (353 K for industrial fuel cell operation), as shown in Figure 7. Initially, the O_2 was set above 3 Å from the catalyst and it was found that O_2 gradually approached the $FeNiN_6$-Gra catalyst and eventually adsorbed on the surface, while a similar phenomenon was found for the $FeNiN_6B1$-Gra catalyst, indicating that O_2 can spontaneously adsorb on the catalyst surface to participate in the ORR reaction at the fuel cell operating temperature.

The obtained results confirm that B-doping significantly increases the onset potential of $FeNiN_6$-Gra, which indicates that $FeNiN_6B1$-Gra is a promising thermodynamically stable ORR catalyst. Therefore, we investigated the kinetic properties of $FeNiN_6$-Gra and $FeNiN_6B1$-Gra. The energy potentials of these two catalysts were calculated according to the four electronic reaction steps (a–d), as shown in Figure 8.

The analysis shows that the energy barriers of steps (a), (b), (c), and (d) in the $FeNiN_6$-Gra-catalyzed ORR process are 0.05, 0.08, 0.50, and 0.28 eV, respectively. Therefore, the hydrogenation of *O to form *OH is the rate-determining step (energy barrier of 0.50 eV). Meanwhile, the steps involved in the $FeNiN_6B1$-Gra-catalyzed ORR process exhibit energy barriers in the range of 0.09–0.54 eV, where the energy barrier of the fourth electron step is 0.17 eV. The rate-determining step in this process is also the hydrogenation of *O. Notably, the energy barrier of this step (0.54 eV) is much

https://doi.org/10.1021/acsomega.2c01415
ACS Omega 2022, 7, 19676–19686

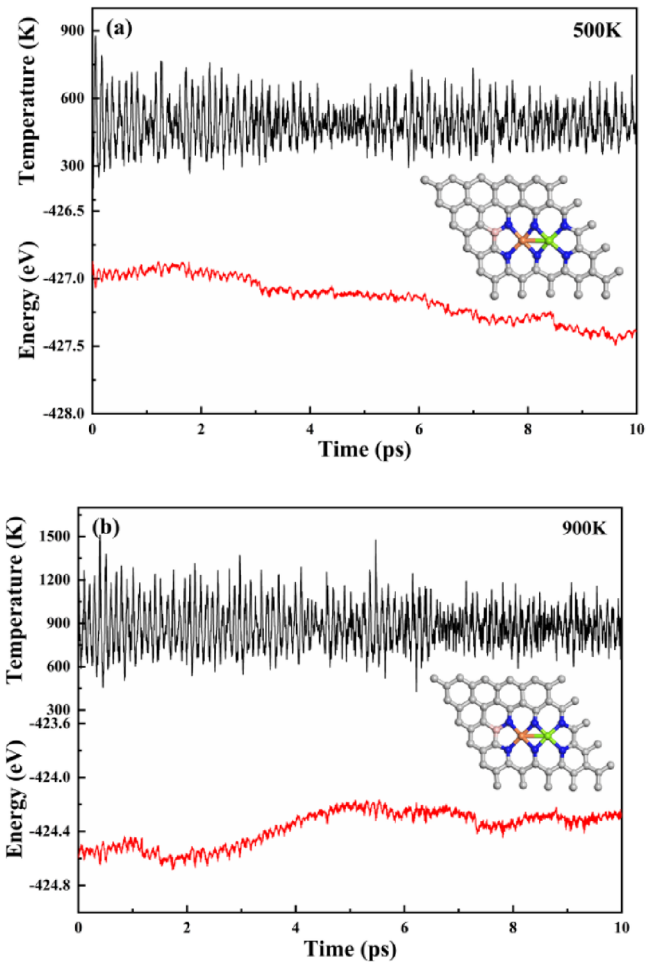

Figure 9. Change in the total energy of $FeNiN_6B1$-Gra and the structural diagram of the catalyst after 10 ps of MD simulation at (a) 500 K and (b) 900 K.

smaller than that of the rate-determining step in the Pt-catalyzed ORR process (0.80 eV[37]). In addition, B-doping of $FeNiN_6$-Gra reduces the energy barrier (by 0.11 eV) for the *OH hydrogenation of the thermodynamically rate-determining step, which confirms that $FeNiN_6B1$-Gra has good catalytic performance on a kinetic level.

The MD simulation conducted herein shows that $FeNiN_6B1$-Gra is stable dynamically. Based on MD simulations performed at 500 and 900 K for 10 ps (Figure 9), the energy of this catalyst oscillates back and forth within a certain range, and no bonds are broken or formed during the simulation, which indicates that $FeNiN_6B1$-Gra is stable dynamically.

CONCLUSIONS

This study investigates the efficiency of ORR catalysts for dual-metal active sites mediated by p-block elements. Replacement of C atoms around the active site with B atoms regulates the intensity of adsorption of oxygen-containing intermediates by changing the total charge of the metal atom at the adsorption site and the four surrounding N atoms, the catalytic activity and onset potential may be increased, and the energy barrier of the rate-determining step may be lowered. The volcano diagram of ORR catalytic activity shows that B-doping of $FeMN_6$-Gra (M = Mn, Ni, Co, or Cu) enhances catalytic performance and that $FeNiN_6B1$-Gra exhibits the greatest enhancement, with a 0.28 V increase in onset potential. Compared to $FeNiN_6$-Gra (energy barrier of 0.28 eV), the energy barrier of the $FeNiN_6B1$-Gra-catalyzed fourth electronic step (0.17 eV) is lower. $FeCoN_6B3$-Gra also shows high catalytic activity, and its onset potential (0.97 V) is even better than that of the Pt catalyst (0.78 V). Overall, the results demonstrate that B-doped double-transition metal electrocatalysts are promising ORR catalysts that merit further theoretical and experimental investigation.

ASSOCIATED CONTENT

Supporting Information

The Supporting Information is available free of charge at https://pubs.acs.org/doi/10.1021/acsomega.2c01415.

DFT calculations of the optimized model and Gibbs free energy values for the adsorption of oxygen-containing intermediates by structures (PDF)

AUTHOR INFORMATION

Corresponding Author

Hong Cui − *School of Mechanical Engineering and Shaanxi Key Laboratory of Industrial Automation, Shaanxi University of Technology, Hanzhong, Shaanxi 723001, China;* orcid.org/0000-0003-0537-5533; Email: hongcui@snut.edu.cn

Authors

Pengyue Shan − *School of Mechanical Engineering and Shaanxi Key Laboratory of Industrial Automation, Shaanxi University of Technology, Hanzhong, Shaanxi 723001, China*

Xue Bai − *School of Mechanical Engineering and Shaanxi Key Laboratory of Industrial Automation, Shaanxi University of Technology, Hanzhong, Shaanxi 723001, China*

Qi Jiang − *School of Mechanical Engineering and Shaanxi Key Laboratory of Industrial Automation, Shaanxi University of Technology, Hanzhong, Shaanxi 723001, China*

Yunjian Chen − *School of Mechanical Engineering and Shaanxi Key Laboratory of Industrial Automation, Shaanxi University of Technology, Hanzhong, Shaanxi 723001, China*

Yazhou Wang − *School of Mechanical Engineering and Shaanxi Key Laboratory of Industrial Automation, Shaanxi University of Technology, Hanzhong, Shaanxi 723001, China*

Tong Liu − *School of Mechanical Engineering and Shaanxi Key Laboratory of Industrial Automation, Shaanxi University of Technology, Hanzhong, Shaanxi 723001, China*

Rong Feng − *School of Mechanical Engineering and Shaanxi Key Laboratory of Industrial Automation, Shaanxi University of Technology, Hanzhong, Shaanxi 723001, China*

Qin Kang − *School of Mechanical Engineering and Shaanxi Key Laboratory of Industrial Automation, Shaanxi University of Technology, Hanzhong, Shaanxi 723001, China*

Zhiyong Liang − *School of Mechanical Engineering and Shaanxi Key Laboratory of Industrial Automation, Shaanxi University of Technology, Hanzhong, Shaanxi 723001, China*

Hongkuan Yuan − *School of Physical Science and Technology, Southwest University, Chongqing 400715, China;* orcid.org/0000-0002-2075-9327

https://doi.org/10.1021/acsomega.2c01415
ACS Omega 2022, 7, 19676−19686

Complete contact information is available at:
https://pubs.acs.org/10.1021/acsomega.2c01415

Author Contributions

The manuscript was written through contributions of all authors. All authors have given approval to the final version of the manuscript.

Notes

The authors declare no competing financial interest.

■ ACKNOWLEDGMENTS

This research was funded by the National Natural Science Foundation of China (nos. 61701288 and 51706128), Basic Research Plan of Natural Science in Shaanxi Province (no. 2021JM-485), Key Scientific Research Project of the Shaanxi Provincial Education Department (no. 20JS019), and Postgraduate Innovation Project of Shaanxi University of Technology (no. SLGYCX2125).

■ REFERENCES

(1) Steele, B. C. H.; Heinzel, A. Materials for fuel-cell technologies. *Nature* **2001**, *414*, 345−352.
(2) Bashyam, R.; Zelenay, P. A class of non-precious metal composite catalysts for fuel cells. *Nature* **2006**, *443*, 63−66.
(3) Debe, M. K. Electrocatalyst approaches and challenges for automotive fuel cells. *Nature* **2012**, *486*, 43−51.
(4) Kulkarni, A.; Siahrostami, S.; Patel, A.; Nørskov, J. K. Understanding Catalytic Activity Trends in the Oxygen Reduction Reaction. *Chem. Rev.* **2018**, *118*, 2302−2312.
(5) Gasteiger, H. A.; Panels, J. E.; Yan, S. G. Dependence of PEM fuel cell performance on catalyst loading. *J. Power Sources* **2004**, *127*, 162−171.
(6) Stamenkovic, V. R.; Mun, B. S.; Arenz, M.; Mayrhofer, K. J. J.; Lucas, C. A.; Wang, G.; Ross, P. N.; Markovic, N. M. Trends in electrocatalysis on extended and nanoscale Pt-bimetallic alloy surfaces. *Nat. Mater.* **2007**, *6*, 241−247.
(7) Wanjala, B. N.; Fang, B.; Luo, J.; Chen, Y.; Yin, J.; Engelhard, M. H.; Loukrakpam, R.; Zhong, C.-J. Correlation between Atomic Coordination Structure and Enhanced Electrocatalytic Activity for Trimetallic Alloy Catalysts. *J. Am. Chem. Soc.* **2011**, *133*, 12714−12727.
(8) Qiao, B.; Wang, A.; Yang, X.; Allard, L. F.; Jiang, Z.; Cui, Y.; Liu, J.; Li, J.; Zhang, T. Single-atom catalysis of CO oxidation using Pt1/FeOx. *Nat. Chem.* **2011**, *3*, 634−641.
(9) Yang, X.-F.; Wang, A.; Qiao, B.; Li, J.; Liu, J.; Zhang, T. Single-Atom Catalysts: A New Frontier in Heterogeneous Catalysis. *Acc. Chem. Res.* **2013**, *46*, 1740−1748.
(10) Lu, Z.; Xu, G.; He, C.; Wang, T.; Yang, L.; Yang, Z.; Ma, D. Novel catalytic activity for oxygen reduction reaction on MnN4 embedded graphene: A dispersion-corrected density functional theory study. *Carbon* **2015**, *84*, 500−508.
(11) Li, T.; Deng, H.; Liu, J.; Jin, C.; Song, Y.; Wang, F. First-row transition metals and nitrogen co-doped carbon nanotubes: The exact origin of the enhanced activity for oxygen reduction reaction. *Carbon* **2019**, *143*, 859−868.
(12) Chen, X.; Yu, L.; Wang, S.; Deng, D.; Bao, X. Highly active and stable single iron site confined in graphene nanosheets for oxygen reduction reaction. *Nano Energy* **2017**, *32*, 353−358.
(13) Fu, X.; Choi, J.-Y.; Zamani, P.; Jiang, G.; Hoque, M. A.; Hassan, F. M.; Chen, Z. Co−N Decorated Hierarchically Porous Graphene Aerogel for Efficient Oxygen Reduction Reaction in Acid. *ACS Appl. Mater. Interface* **2016**, *8*, 6488−6495.
(14) Zhang, X.; Yang, Z.; Lu, Z.; Wang, W. Bifunctional CoNx embedded graphene electrocatalysts for OER and ORR: A theoretical evaluation. *Carbon* **2018**, *130*, 112−119.
(15) Wang, J.; Huang, Z.; Liu, W.; Chang, C.; Tang, H.; Li, Z.; Chen, W.; Jia, C.; Yao, T.; Wei, S.; et al. Design of N-Coordinated Dual-Metal Sites: A Stable and Active Pt-Free Catalyst for Acidic Oxygen Reduction Reaction. *J. Am. Chem. Soc.* **2017**, *139*, 17281−17284.
(16) Meng, Y.; Yin, C.; Li, K.; Tang, H.; Wang, Y.; Wu, Z. Improved Oxygen Reduction Activity in Heteronuclear FeCo-Codoped Graphene: A Theoretical Study. *ACS Sustainable Chem. Eng.* **2019**, *7*, 17273−17281.
(17) Hu, R.; Li, Y.; Zeng, Q.; Shang, J. Role of active sites in N-coordinated Fe-Co dual-metal doped graphene for oxygen reduction and evolution reactions: A theoretical insight. *Appl. Surf. Sci.* **2020**, *525*, No. 146588.
(18) Gong, S.; Wang, C.; Jiang, P.; Hu, L.; Lei, H.; Chen, Q. Designing highly efficient dual-metal single-atom electrocatalysts for the oxygen reduction reaction inspired by biological enzyme systems. *J. Mater. Chem. A* **2018**, *6*, 13254−13262.
(19) Xu, J.; Elangovan, A.; Li, J.; Liu, B. Graphene-Based Dual-Metal Sites for Oxygen Reduction Reaction: A Theoretical Study. *J. Phys. Chem. C* **2021**, *125*, 2334−2344.
(20) Wang, F.; Xie, W.; Yang, L.; Xie, D.; Lin, S. Revealing the importance of kinetics in N-coordinated dual-metal sites catalyzed oxygen reduction reaction. *J. Catal.* **2021**, *396*, 215−223.
(21) Wang, M.; Yang, W.; Li, X.; Xu, Y.; Zheng, L.; Su, C.; Liu, B. Atomically Dispersed Fe−Heteroatom (N, S) Bridge Sites Anchored on Carbon Nanosheets for Promoting Oxygen Reduction Reaction. *ACS Energy Lett.* **2021**, *6*, 379−386.
(22) Qi, W.; Huang, W.; Niu, J.; Zhang, B.; Zhang, Z.; Li, W. The role of S in the Co-N-S-C catalysis system towards the ORR for proton exchange membrane fuel cells. *Appl. Surf. Sci.* **2021**, *540*, No. 148325.
(23) Tang, C.; Chen, L.; Li, H.; Li, L.; Jiao, Y.; Zheng, Y.; Xu, H.; Davey, K.; Qiao, S.-Z. Tailoring Acidic Oxygen Reduction Selectivity on Single-Atom Catalysts via Modification of First and Second Coordination Spheres. *J. Am. Chem. Soc.* **2021**, *143*, 7819−7827.
(24) Shang, H.; Zhou, X.; Dong, J.; Li, A.; Zhao, X.; Liu, Q.; Lin, Y.; Pei, J.; Li, Z.; Jiang, Z.; et al. Engineering unsymmetrically coordinated Cu-S1N3 single atom sites with enhanced oxygen reduction activity. *Nat. Commun.* **2020**, *11*, 3049.
(25) Jiang, Z.; Sun, W.; Shang, H.; Chen, W.; Sun, T.; Li, H.; Dong, J.; Zhou, J.; Li, Z.; Wang, Y.; et al. Atomic interface effect of a single atom copper catalyst for enhanced oxygen reduction reactions. *Energy Environ. Sci.* **2019**, *12*, 3508−3514.
(26) Sun, H.; Wang, M.; Du, X.; Jiao, Y.; Liu, S.; Qian, T.; Yan, Y.; Liu, C.; Liao, M.; Zhang, Q.; et al. Modulating the d-band center of boron doped single-atom sites to boost the oxygen reduction reaction. *J. Mater. Chem. A* **2019**, *7*, 20952−20957.
(27) Kresse, G.; Hafner, J. Ab initio molecular-dynamics simulation of the liquid-metal-amorphous-semiconductor transition in germanium. *Phys. Rev. B* **1994**, *49*, 14251−14269.
(28) Kresse, G.; Furthmüller, J. Efficient iterative schemes for ab initio total-energy calculations using a plane-wave basis set. *Phys. Rev. B* **1996**, *54*, 11169−11186.
(29) Kresse, G.; Furthmüller, J. Efficiency of ab-initio total energy calculations for metals and semiconductors using a plane-wave basis set. *Comput. Mater. Sci.* **1996**, *6*, 15−50.
(30) Blöchl, P. E. Projector augmented-wave method. *Phys. Rev. B* **1994**, *50*, 17953−17979.
(31) Perdew, J. P.; Burke, K.; Ernzerhof, M. Generalized Gradient Approximation Made Simple. *Phys. Rev. Lett.* **1996**, *77*, 3865−3868.
(32) Monkhorst, H. J.; Pack, J. D. Special points for Brillouin-zone integrations. *Phys. Rev. B* **1976**, *13*, 5188−5192.
(33) Grimme, S.; Antony, J.; Ehrlich, S.; Krieg, H. A consistent and accurate ab initio parametrization of density functional dispersion correction (DFT-D) for the 94 elements H-Pu. *J. Chem. Phys.* **2010**, *132*, 154104.
(34) Henkelman, G.; Uberuaga, B. P.; Jónsson, H. A climbing image nudged elastic band method for finding saddle points and minimum energy paths. *J. Chem. Phys.* **2000**, *113*, 9901−9904.
(35) Elstner, M.; Porezag, D.; Jungnickel, G.; Elsner, J.; Haugk, M.; Frauenheim, T.; Suhai, S.; Seifert, G. Self-consistent-charge density-

functional tight-binding method for simulations of complex materials properties. *Phys. Rev. B* **1998**, *58*, 7260−7268.
(36) Nørskov, J. K.; Rossmeisl, J.; Logadottir, A.; Lindqvist, L.; Kitchin, J. R.; Bligaard, T.; Jónsson, H. Origin of the Overpotential for Oxygen Reduction at a Fuel-Cell Cathode. *J. Phys. Chem. B* **2004**, *108*, 17886−17892.
(37) Duan, Z.; Wang, G. Comparison of Reaction Energetics for Oxygen Reduction Reactions on Pt(100), Pt(111), Pt/Ni(100), and Pt/Ni(111) Surfaces: A First-Principles Study. *J. Phys. Chem. C* **2013**, *117*, 6284−6292.

https://doi.org/10.1021/acsomega.2c01415
ACS Omega 2022, 7, 19676−19686